

Probability Map Guided Bi-directional Recurrent UNet for Pancreas Segmentation

Jun Li[†], Xiaozhu Lin[†], Hui Che, Hao Li, and Xiaohua Qian^{*}

Abstract—Pancreatic cancer is one of the most lethal cancers as morbidity approximates mortality. A method for accurately segmenting the pancreas can assist doctors in the diagnosis and treatment of pancreatic cancer, but huge differences in shape and volume bring difficulties in segmentation. Among the current widely used approaches, the 2D method ignores the spatial information, and the 3D model is limited by high resource consumption and GPU memory occupancy. To address these issues, we propose a bi-directional recurrent UNet based on probabilistic map guidance (PBR-UNet). PBR-UNet includes a feature extraction module for extracting pixel-level probabilistic maps and a bi-directional recurrent module for fine segmentation. The extracted probabilistic map will be used to guide the fine segmentation and bi-directional recurrent module integrates contextual information into the entire network to avoid the loss of spatial information in propagation. By combining the probabilistic map of the adjacent slices with the bi-directional recurrent segmentation of intermediary slice, this paper solves the problem that the 2D network loses three-dimensional information and the 3D model leads to large computational resource consumption. We used Dice similarity coefficients (DSC) to evaluate our approach on NIH pancreatic datasets and eventually achieved a competitive result of 83.35%.

Index Terms—Pancreas segmentation, Deep learning, Medical image segmentation

I. INTRODUCTION

In traditional pancreatic cancer surgery, surgeons usually judge the anatomical structure of the human body by experience. However, due to the huge difference in the shape of the pancreas and the vulnerability to the elastic deformation such as breathing and heartbeat, it is much hard to locate the pancreas. Therefore, exploring the automatic segmentation of the pancreas is of great significance for accuracy improvement and risk reduction of computer-assisted diagnosis techniques. Compared with kidney, heart or liver in which segmentation can reach more than 90% accuracy by calculating DSC [1], [2], pancreas present the smaller volume fraction and high anatomical variability as [3] and Figure 1 (a) show, which

J. Li, H. Li, and X. Qian, are with the School of Biomedical Engineering, Shanghai Jiaotong University, Shanghai 200240, China (e-mail: dirk.li@outlook.com; haoli@sjtu.edu.cn; xiaohua.qian@sjtu.edu.cn)

X. Lin is the Ruijin Hospital, Shanghai Jiaotong University School of Medicine, Shanghai 200240, China.

H. Che is Biomedical Engineering Department, Rutgers University, New Jersey 08901, USA (e-mail: hui.che@rutgers.edu)

[†] J. Li and X. Lin contributed equally.

^{*}Xiaohua Qian is the corresponding author.

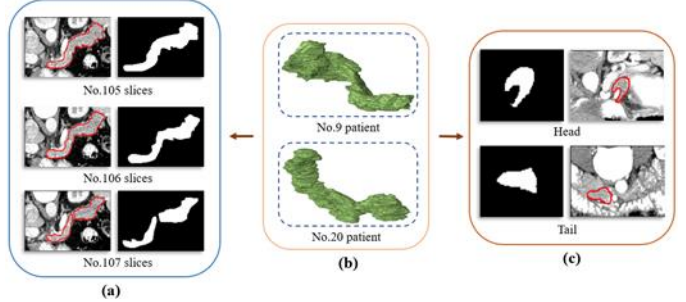


Fig. 1. Examples of CT scans showing pancreas. (a) indicates that the adjacent three-slice pancreas has a great correlation; (b) indicates that the pancreas of different individuals has different spatial shapes; (c) indicates the significant difference in shape between the head and tail of the patient's pancreas.

prevents many segmentation methods from achieving high precision [4], making the model easily disturbed by background tissue and dramatic volume changes. Therefore, the pancreas has always been considered one of the most difficult types of organ segmentation [5], [6].

In recent years, with the development of deep learning techniques, more and more researchers began to use natural image semantic segmentation model to operate medical image segmentation tasks. Many excellent semantic segmentation models have been proposed such as FCN [7], UNet [8], DeepLab [9]. The structure of Encoder-Decoder is widely used in medical image segmentation, because skip connection has been proved to be helpful to restore the full spatial resolution of network output, making the full convolution method suitable for semantic segmentation [10], [11]. It turns out that a network with this structure not only increases the final output resolution but also enables accurate positioning. Both contribute to detecting the semantic information of the target organization in the whole slice, which means the difference between the target organization and other organizational features. And more precise functional details than FCN can be obtained through the Encoder.

Most of existing approaches for segmentation with deep learning techniques are based on two-dimensional data, that each slice of an organ is viewed as an object for segmentation. After segmentation for all slices, recombination is performed to generate the segmented three-dimensional organ [5], [12], [13]. But in clinical diagnostics, experienced radiologists usually observe and segment the target tissue according to many adjacent slices along the Z axis [14]. The severe problem of this approach is to ignore the contextual information on the Z axis of the organ. All these networks are shallow and ignore the 3D contexts, which limit the high-level feature extraction capabil-

ity and restrict the recognition performance [14].

Also some researchers use 3D models to directly treat all slices of a patient as a segmentation object [15]–[21], which considers the advantage of the three-dimensional information of the organ. However, this approach relies excessively on computing resources and high requirements for hardware devices [14], [22], resulting in high computational cost and GPU memory footprint. High memory footprint limits the depth of the network and the field of view of the filter, which is precisely the two key factors for performance improvement [23]. In [24], researchers evaluated a complete 3D convolutional architecture and found that it provided a slightly higher result than the previous method, but the cost is significant increase in computational capacity requirements. This method is possible to lower the result due to no direct relation between the head and tail of the pancreas which can be seen from figure 1(a), and no correlation in shape may mislead segmentation results by dramatic shape changes in the pancreas. However, the similarity of adjacent slices is high and the difference of the target tissue in adjacent slices is relatively small, so adjacent slices within a certain range are capable of guiding the segmentation of each slice.

The volume of the pancreas is small so most region of the image is the background, and a single segmentation may cause results biased towards the background. Thus, some researchers begin to employed the cascaded learning strategy [18], [25]–[28]. The main thought of the method is to locate pancreatic region by rough approximate segmentation at first, then fine segmentation is carried out in the target area. With the rough result acquired from the first step, most of the background interference can be removed, allowing the model to focus on a specific range for segmentation. However, in the first step the model will not only remove background interference but also possibly remove the target tissue. This loss is irreversible. [29] shows two failed examples using the method proposed in [5]. In some cases, the output of DSC is extreme low or even 0. In this complicated situation, positioning result is usually unreliable and unstable due to lack of an effective error correction mechanism. Besides, it is generally difficult to utilize the third dimension of information in fine segmentation, resulting in inaccurate segmentation performance [3].

After bi-directional long short-term memory (BiLSTM) achieved great success in text analysis, researchers employed it to deal with the medical image segmentation task [30], [31]. This strategy treats the context information of the pancreas as a sequence, and the context information is given to different nodes in the BiLSTM, which can optimize segmentation results with spatial information. The drawback of this strategy is still the tortuosity of the pancreas shape may lead to wrong guidance. For example, if using the pancreatic head to guide the pancreatic tail, the result will greatly deviate. Moreover, for LSTMs-based models, it is connected as a separate refine module behind the segmentation networks [30], which has little contribution to the result but makes the entire network larger and more difficult to converge. Therefore, considering the computational resources it consumes, the contribution of the LSTMs-based models is limited.

In this paper, we propose a more efficient network of bi-directional recurrent segmentation based on probabilistic map guidance. The proposed method can improve the efficiency of the utilization of spatial information, thus, it can solve the problem of high demand for hardware equipment when using three-dimensional information. Firstly, we use the standard UNet model to extract the pixel-level probabilistic map in each slice, which represents the probability of each pixel belonging to the pancreatic tissue. This probabilistic map generated just identify the approximate location of pancreatic tissue in each slice and does not guarantee accuracy. Innovatively, we use it as the guidance of fine segmentation. As shown in Figure 1(a), the adjacent slices have a strong correlation, so we constrain the segmentation of intermediate slices with the position information of adjacent slices for patching and optimizing pixels that were incorrectly segmented in the first step. It makes up for the shortcomings of using a binary map, which describe only the outlines but no details. Then, We use a multi-channel network to integrate intra-slice information and contexts information, which proved to be better than a single-channel network without increasing the computational burden [24]. In the integration process, adjacent slices play key roles in the segmentation results of intermediary slice and mutual effect will be transmitted in all slices. To enable this interaction to propagate through the network and get better results, we add an iterative process of bi-directional recurrent to optimize and update the probabilistic maps in each propagation process. In the bi-directional recurrent segmentation, under the guidance of increasingly accurate contextual information, the burden of searching for the optimal pancreatic region is well-relieved and results can achieve high precision. What's more, this work does not rely on any pre-training model, just relates to the generalization of the model itself.

II. METHODOLOGY

In this paper, we proposed a probabilistic map guided bi-directional recurrent UNet (PBR-UNet) for pancreas segmentation, which is shown in Figure 2. PBR-UNet aims to combine the probabilistic map of the adjacent slices with the bi-directional recurrent segmentation of intermediary slice to solve the problem that the 2D network loses three-dimensional information and the 3D model leads to large computational resource consumption. PBR-UNet first obtains a rough pixel-level probabilistic map by feature extraction model. The original image is then combined with the probabilistic map of the adjacent slices to form the segmentation guidance. As a result, the context information can be used to limit and guide the segmentation of interlayer slice. Because of the interaction between adjacent slices to form an interlocking structure, we use recurrent in both forward and reverse two directions to propagate context information throughout the entire segmentation process. What's more, we use iterators to optimize the transfer process so that each propagation can update the probabilistic map to make it more accurate. These measures ensure that the final output is obtained through global optimal three-dimensional information guidance. Specific details about PBR-UNet will be introduced in the following sections.

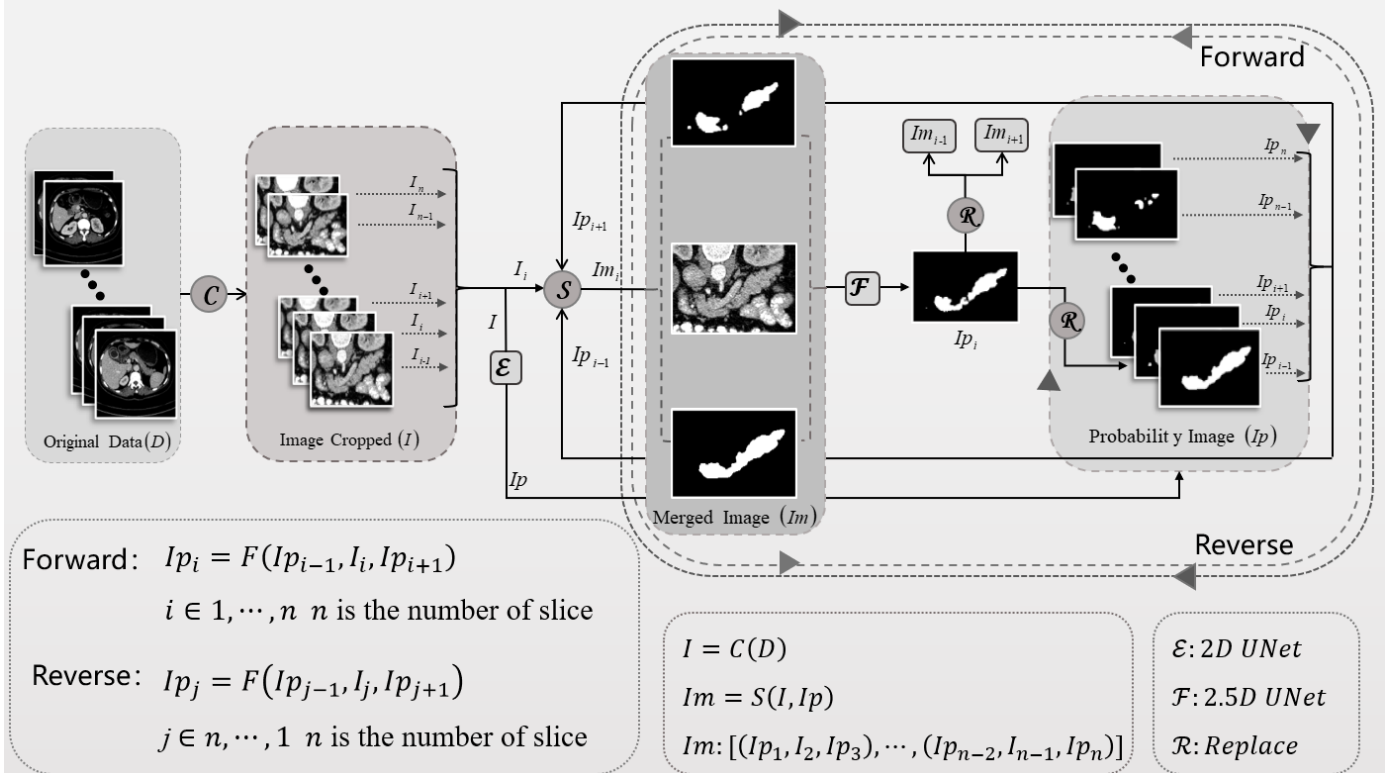


Fig. 2. The illustrations of PBR-UNet. We use Ip and I to represent the probabilistic map and the original image respectively, Ip and I are combined into multi-channel data Im by function S . The function E represents a 2D network for extracting probabilistic maps. The input of function E is 3D scan, and the output is the probability that each pixel belongs to the pancreatic tissue. The function F represents the bi-directional recurrent segmentation process in the second part, and the input of F is Im_i . Correspondingly, the output of F is Ip_i which updates the corresponding parts of Im_{i-1} , Im_{i+1} and Ip_i to increase the accuracy of the guidance. The update process mentioned above is represented by R , and it is worth mentioning that these processes are circular and will not end until the threshold is reached.

A. Problem Define and Inference Schemes

Our main task is to segment the pancreas tissue from the 3D scan accurately, and the problem can be defined as follows. Given a patient's three-dimensional scan data $P \in R^{m \times h \times w}$, where m denotes the total number of slices, h and w respectively refers to the height and width of the image. Moreover, the ground truth map $\hat{Y} \in R^{m \times h \times w}$ is provided. These data are used to train a mapping function Ω to segment the pancreas from the given CT three-dimensional scan. In this process, it is necessary to make the similarity between $\Omega(P)$ and ground truth map \hat{Y} as high as possible. The mapping function Ω contains two parts: \mathcal{E} and \mathcal{F} . The function \mathcal{E} denotes the feature extraction model, which get the pixel-level probabilistic map of each slice in the 3D scan; The function \mathcal{F} denotes the bi-directional recurrent segmentation model. The threshold T is the maximum number of cycles, θ is the threshold of evaluation, pixels with probability value greater than θ will be considered to belong to the pancreatic tissue. We can use the following equation to explain the above process:

$$\mathcal{L}(\Omega, \theta, T; P, \hat{Y}) = \min \left(\frac{1}{m} \sum_{i=1}^m \left(\mathcal{F}(\mathcal{E}(P_i); \theta, T) - \hat{Y}_i \right)^2 \right) \quad (1)$$

To make full use of the 3D information of the pancreas, we combine the pixel-level probabilistic map Ip with the original data I . Im denotes the generated data that synthesized from groups Ip and I , simultaneously is used as the input in the next segmentation process \mathcal{F} . The multi-channel data Im interact

with each other. Because of the interaction, an inter-locking structure is formed in multi-channel data Im . To introduce the multi-dimensional information into the model, the precise segmentation \mathcal{F} is designed to contain positive and reverse two directions. When performing forward segmentation, the initial slice just has the information of next slice, but no information of the previous slice, and the case is reversed when this proceeding to the last slice. Therefore, in order to overcome the loss of adjacent slice information at the edge, we designed a bi-directional recurrent segmentation method, which can be expressed as Formula 2, and the detailed procedure will be described in section B and C.

$$\Omega(P) = \sum_l (reverse_l(forward_l(P))) \quad (2)$$

B. Extraction and Combination of Probabilistic Maps

In this section, we use a 2D UNet network to extract the probabilistic map. The networks with skip connections like UNet have been proven to help restore the full spatial resolution of the network output. As a result, the full convolution method is considered to be extremely suitable for semantic segmentation [10], [11]. Specifically, the structure with skip connection enables deep and shallow information to be obtained. In this paper, the positional information of the pancreatic tissue and the geometrical shape of the surrounding tissue can be considered as the semantic information, which could be obtained by continuous downsampling. Generally, the target tissues can be roughly distinguished with the obtained

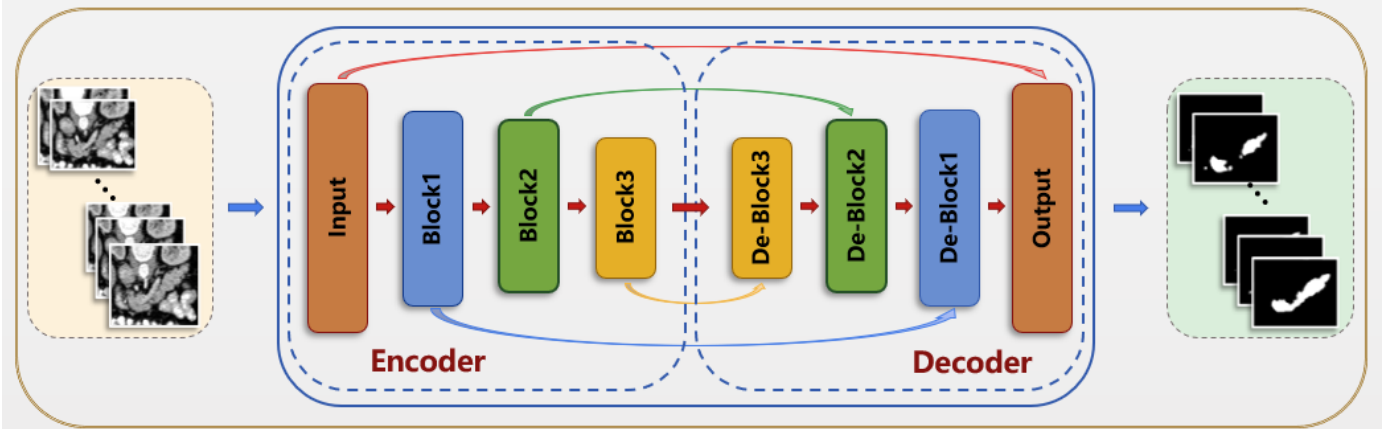


Fig. 3. The illustrations of probabilistic map extraction framework (best viewed in color). Encoder and Decoder are four layers, all of which are directly connected. The activation function is omitted, and the output layer is 1x1. Then the sigmoid activation function is used to obtain the probability that each pixel belongs to pancreatic tissue.

information, so it is often used in classification tasks [23], [32], [33]. However, for semantic segmentation, these features are not enough, so skip connection is added to get the shallow information. The high-resolution information is directly passed from the Encoder to the Decoder by skip connection. More features that are precise become available for semantic segmentation. Thus, we trained a full convolutional network with skip connection proposed in [8], to quickly extract intra-slice features in 3D scan and characterize them with probabilistic values.

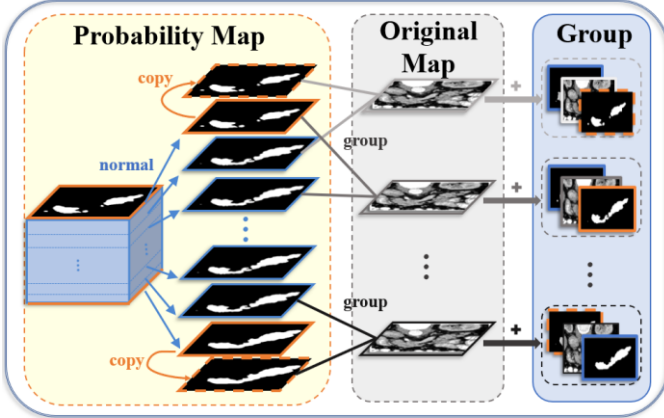


Fig. 4. The illustrations of converting volume data to multi-channel data. The initial slice has only the information of the next slice, but no information of the previous slice, and the case is reversed when this proceeding to the last slice, so we copy the initial slice and the last slice as their context information.

Let $I \in R^{m \times h \times w \times c}$ denote the input training samples, in which c is the number of channels. As shown in Equation 3, $\hat{Y}_{i,j,k,\cdot}$ denotes the ground truth map of the data, and the value is 0 or 1, 1 means the pixel belongs to pancreas tissue and 0 means is opposite.

$$\hat{Y}_{i,j,k,\cdot} = \begin{cases} 0, & (i,j,k,\cdot) \notin \text{pancreas} \\ 1, & (i,j,k,\cdot) \in \text{pancreas} \end{cases} \quad (3)$$

Without loss of generality, 2D segmentation network along the Z-axis is applied in the probabilistic map extraction model. In this step, an accurate binary segmentation is not necessary, and we just get the probabilistic map Ip of each pixel. As

shown in Fig 2, the function \mathcal{E} is a full convolutional network with a skip connection, to complete a conversion from volume data to a pixel-level probabilistic map, which could be expressed by the following Equation 4:

$$Ip_\vartheta = \mathcal{E}(I) \quad (4)$$

$$I \& Ip_\vartheta \in R^{m \times h \times w \times c}, \|Ip_\vartheta\| \in [0, 1]$$

After obtaining the probabilistic map Ip_ϑ , the original data I and the probabilistic map Ip_ϑ are combined into three-channel data through the transformation S . The method in [14] is to use three adjacent slices of original data on the Z-axis. Due to uncertainty of prediction, some information would be lost and the efficiency of using context information would be reduced. Here we use pixel-level probabilistic map to replace the upper and lower slices of the three adjacent slices in [14]. Based on this operation, there will be neither absolute threshold caused by mask guidance nor uncertain loss of information. The multi-channel data obtained by the combination is denoted by $Im_\vartheta \in R^{m \times h \times w \times c}$, and the conversion process can be expressed by Equation 5, 6. It should be noticed that since the initial slice does not have the upper slice, and the last slice does not have the lower slice, we copy the initial and the final slice then add them to Ip_ϑ . The process of this combination is shown in Figure 4.

$$Im_\vartheta = S(I, Ip_\vartheta), Im_\vartheta \in R^{m \times h \times w \times c} \quad (5)$$

$$Im_\vartheta = \left[(Ip_{\vartheta,1}, I_1, Ip_{\vartheta,2}), (Ip_{\vartheta,1}, I_2, Ip_{\vartheta,3}), \dots \right. \\ \left. \dots, (Ip_{\vartheta,n-1}, I_n, Ip_{\vartheta,n}) \right] \quad (6)$$

The generated data is subjected to bi-directional recurrent segmentation by 2.5D UNet under the guidance of probabilistic map. The 2.5D network here adopts the same structure as probabilistic map extraction model, and the number of data channels is modified to c , the parameters in the network are not shared so separate training is required.

The overall structure of 2D UNet and 2.5DUNet is shown in Figure 4. Encoder module and Decoder module are both four layers, and all layers are directly connected. To control the number of feature maps and prevent feature map expansion, we use the base factor ϖ , and each layer performs a multiple conversion based on the base factor ϖ . The UpSampling layer is implemented by deconvolution rather than upsampling.

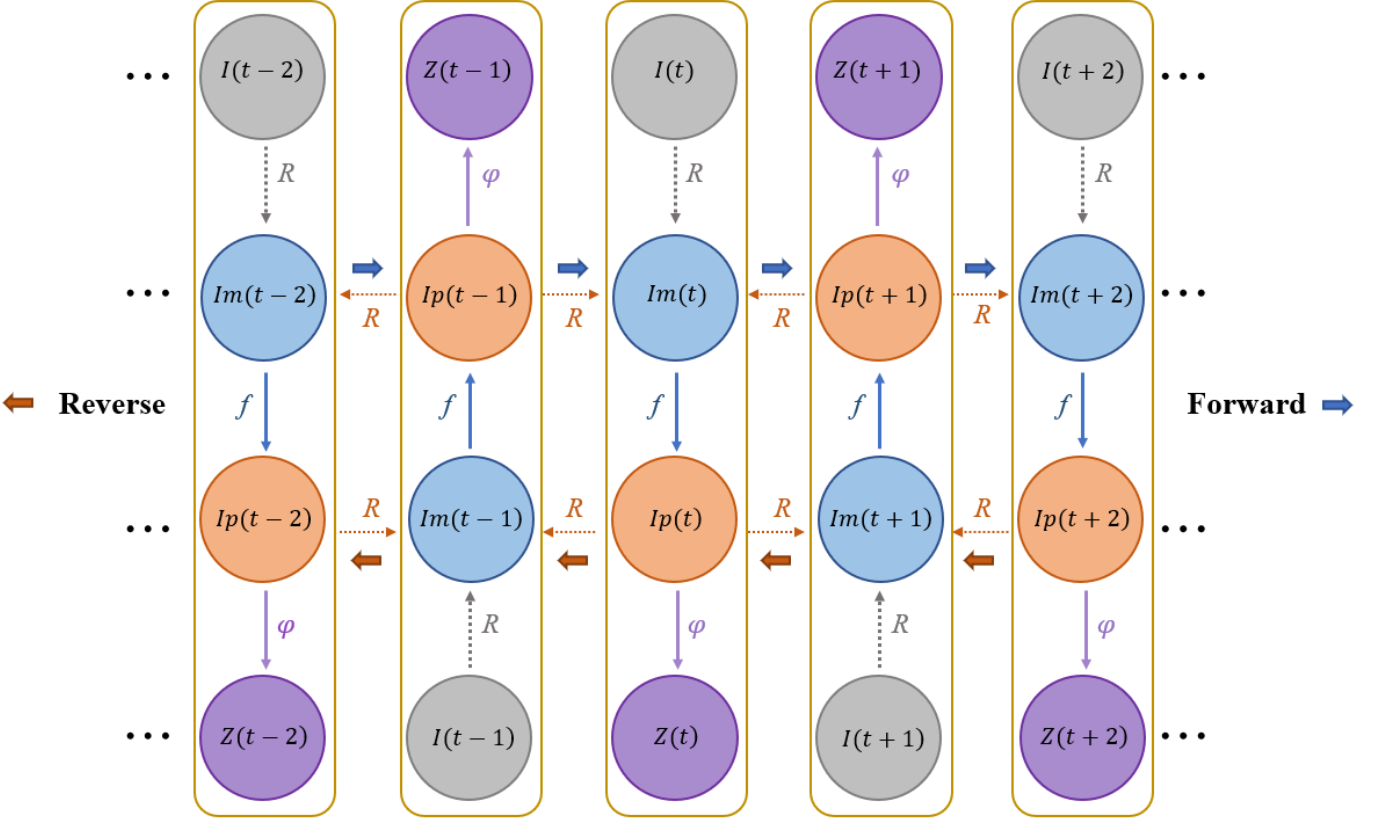


Fig. 5. The illustration of the pipeline for bi-directional recurrent segmentation. Segmentation under the guidance of context information allows operating a single model f on all synchronization sequences of the recurrent segmentation, no need to set up a separate model that is synchronized with time. The training samples and duration required for the bi-directional recurrent model will be much less than the model without parameter sharing.

Upsampling can be regarded as the reverse operation of pooling, using nearest neighbor interpolation to zoom in. The method of directly copying the data of rows and columns to expand the size of the feature map may cause abnormal feature distribution [34]. Therefore, we use deconvolution instead of it. The output of the deconvolution is skip-connected with the corresponding shallow feature (Encoder part) and passed through two 3×3 convolutional layers. The details of the 2.5D bi-directional recurrent segmentation will be covered in next section.

C. Bi-directional Recurrent segmentation

A full convolution network with skip connections trained for extracting probabilistic map can capture intra-slice features but is powerless to extract the Z-axis-based contextual information that doctors usually refer. What is more, 3D networks like [16]–[20], [34] have large GPU computing cost and limited kernel view and network depth [14]. Given that the pancreatic context information is not overall relevant, we propose to use the probabilistic map to represent the context information in a specific range to guide the bi-directional recurrent segmentation.

Figure 3 shows the process of how to combine the probabilistic map with the original image. In Equation 7, we can find the generated Im_i , Im_{i-1} and Im_{i+1} are associated in some channels, which creates a chain-like structure. Just like the principle of transmission, we hope this structure can transfer three-dimensional information in the network to help segmentation. We use the two-way propagation method here,

spreading relevant information in two directions. It avoids loss of the corresponding context information due to loss of the propagation process. All of these ensure that the spatial information currently propagating in the network will be fully integrated during the segmentation process. When spatial information spread in chains in the network, an iterative optimizer is added to adjust and optimize spatial information during the transfer process. During the propagation process, the corresponding probabilistic map will be updated at the end of each propagation, making the probabilistic map more accurate. It ensures that the final output is guided by the global optimal three-dimensional information.

$$f(Ip_{i-1}, I_i, Ip_{i+1}) = \\ f(f(Ip_{i-2}, I_{i-1}, Ip_i), I_i, f(Ip_i, I_{i+1}, Ip_{i+2})) = f(\dots) \quad (7)$$

We can consider the chain structure mentioned above as a recurrent neural network, just as almost all functions can be regarded as a feedforward network. Any function involving a loop can be regarded as a recurrent neural network [35]. Considering the chain structure mentioned above as a recurrent neural network has the following two advantages [35]: **a**) The model always has the same input size because it only transfers from one probability distribution state to another; **b**) We can use the same transfer function f of the same parameter on each time step. In this way, we can operate the single model f on all synchronization sequences of the recurrent segmentation, no need to set up a separate model that is synchronized with time.

Considering that the recurrent neural network occupies a large number of resources, to reduce the resource consumption

of the system, we innovatively combine the above recurrent process with 2.5D UNet and propose a bi-directional recurrent network based on pixel-level probabilistic map guidance. Under the guidance of effective context information within a certain range, the burden of searching for the optimal solution of the pancreatic region in the fine segmentation is well-relieved. We compare our proposed model to the classical equation of the recurrent neural network, and we can regard Ip as the hidden unit h in the recurrent neural network.

$$Ip_t = f(Ip_{t-1}, Ip_{t+1}, I_t; \theta) \quad (8)$$

In the classic RNN, the hidden unit generally needs to map a sequence of a certain length ($\dots, x_{t-2}, x_{t-1}, x_{t+1}, x_{t+2}, \dots$) to the unit h_t , especially in statistical language modeling, it is often necessary to store all the information remaining in the sentence [35]. In the work of this paper, if we map a long sequence into the current unit, it will cause the training delay to introduce noise, so we only take the adjacent slice information as the guide.

In the previous section, we introduced how to use the function S to combine the original data I and the probabilistic map Ip_θ into three-channel data Im_θ . To get the binary segmentation of the final output, we first define $\mathcal{F}[\cdot; \theta]$ as a bi-directional recurrent 2.5D UNet network guided by probabilistic maps, where θ is used as a variable parameter for thresholding the output probabilistic map Ip_θ , which can be expressed as Equation 7. The detailed structure of the bi-directional recurrent network based on probabilistic map guidance is shown in Table 1.

$$Z = \mathcal{A}[Ip_\theta \geq 0.5] \quad (9)$$

Now we introduce the workflow of the model. The overall algorithm flow is shown in Algorithm 1. First, we define the variables used in it. The maximum number T of bi-directional recurrent processes is T_{start} times, and the value of θ used for thresholding is θ_{start} .

Forward: When we get the combined data Im_θ from the probabilistic map and the original image in the probabilistic map extractor, we use 2.5D UNet to get the new probabilistic map Ip_ϱ . The difference is that the number of model channels becomes 3. Then we use the function $\mathcal{P}(Ip_\varrho, Ip_\theta)$ to judge whether the new probabilistic map Ip_ϱ generated by the combination probabilistic map Ip_θ is closer to the fine label. If the improvement result is greater than 0, then we can use the newly generated probability map Ip_ϱ to replace the corresponding part of the three-channel data Im_ϱ generated by Ip_ϱ and I , which can be expressed by the following equation, where $Im_{\varrho, i-1}^{(j)}$ represents the channel j in the data $i-1$ in Im_ϱ , and Ip_ϱ will also be updated.

Reverse: After the network completes a forward loop, most of the Ip_θ and Im_ϱ will be updated, but the one-way loop will only get the following information and lose the information of upper slice, so we reverse the same process again, which completes a loop in the bi-directional recurrent segmentation.

$$Im_{\varrho, i-1}^{(3)}, Im_{\varrho, i+1}^{(1)} \leftarrow R(Ip_{\varrho, i}, Im_{\varrho, i-1}^{(3)}, Im_{\varrho, i+1}^{(1)}) \quad (10)$$

D. Loss Function

Since the task is to achieve two-class segmentation with class imbalance, we use the same strategy as [20] to use Dice simi-

larity coefficient (DSC) instead of Cross entropy for training and characterizing similarity. We give the ground truth map \hat{Y} and the final output $\Omega(P)$, then DSC loss can be defined as follows:

$$\begin{aligned} Loss(\Omega(P), \hat{Y}) &= 1 - DSC(\Omega(P), \hat{Y}) \\ &= 1 - \frac{2 \times |\Omega(P) \cap \hat{Y}|}{|\Omega(P)| + |\hat{Y}|} \end{aligned} \quad (11)$$

It can be seen from the above equation that the value of DSC loss is in the range of [0, 1], where 0 represents the completely failed segmentation, and 1 represents the perfect segmentation.

Algorithm 1: Probabilities Guided Bi-directional Recurrent

Input: input volume I , max number of iterations T , probability threshold θ , DSC threshold D ;

Output: segmentation volume Z ;

- 1: $T \leftarrow T_{start}, \theta \leftarrow \theta_{start}, t \leftarrow 0;$
- 2: $Ip_\theta \leftarrow E(I), I, Ip_\theta \in R^{n \times 224 \times 224 \times 1};$
- 3: $Im_\theta \leftarrow S(I, Ip_\theta), Im_\theta \in R^{n \times 224 \times 224 \times 3};$
- 4: **Repeat:**
- 5: **For** $i \leftarrow 0$ to n (forward):
- 6: $Ip_{\varrho, i} \leftarrow F(Im_{\varrho, i}), Im_{\varrho, i} = (Ip_{\varrho, i-1}, I_t, Ip_{\varrho, i+1});$
- 7: **If** $\mathcal{P}(Ip_{\varrho, i}, Ip_{\varrho, i}) > 0:$
- 8: $Im_{\varrho, i-1}^{(2)}, Im_{\varrho, i+1}^{(0)} \leftarrow R(Ip_{\varrho, i}, Im_{\varrho, i-1}^{(2)}, Im_{\varrho, i+1}^{(0)});$
- 9: $Ip_{\varrho, i} \leftarrow R(Ip_{\varrho, i}, Ip_{\varrho, i});$
- 10: **For** $j \leftarrow n$ to 0 (reverse):
- 11: $Ip_{\varrho, j} \leftarrow F(Im_{\varrho, j}), Im_{\varrho, j} = (Ip_{\varrho, j-1}, I_j, Ip_{\varrho, j+1});$
- 12: **If** $\mathcal{P}(Ip_{\varrho, j}, Ip_{\varrho, j}) > 0:$
- 13: $Im_{\varrho, j-1}^{(2)}, Im_{\varrho, j+1}^{(0)} \leftarrow R(Ip_{\varrho, j}, Im_{\varrho, j-1}^{(2)}, Im_{\varrho, j+1}^{(0)});$
- 14: $Ip_{\varrho, j} \leftarrow R(Ip_{\varrho, j}, Ip_{\varrho, j});$
- 15: $Z^{[t]} = \varphi(Ip_\varrho \geq 0.5)$
- 16: $t \leftarrow t + 1$
- 17: **Until** $t = T$ or $DSC\{Z^{[t]}, Y\} \geq D$

Return: $Z \leftarrow Z^{[t]}$

III. EXPERIMENTS AND RESULTS

A. Dataset and Pre-processing

Following previous work of pancreas segmentation [15], we used the most authoritative public dataset NIH pancreatic segmentation dataset [6] to evaluate our method. This dataset contains 82 contrast-enhanced abdominal CT volumes and corresponding fine annotations, the resolution of each CT scan is $512 \times 512 \times L$, where $L \in [181, 466]$ is the number of sampling slices along the long axis of the body. Similar to [3], the images are cropped to [192, 240] and fed into a probabilistic map extraction stage. This process is represented by C . To

assess the robustness of the model, we used 4-fold cross-validation approach in this paper. In our experiment, the dataset is randomly split for training and testing. The data from 62 (approximately 3/4) patients are used for training and the remaining 20 (approximately 1/4) are used for testing. In order to eliminate the effect of randomness, we conduct the operation for 10 times and every time we split the dataset randomly again. As mentioned above, we use the DSC to evaluate the model. To get more comprehensive, we measure the standard deviation, the maximum and minimum values, and calculating the average of all test cases.

The gray value span of initial data is very large, exceeding 2000 gray values. According to prior knowledge, we cut all image intensity values to the range of [-100,200] HU and normalize them to remove the interference from other tissues in the background.

B. Evaluation metrics

We used the dice score to evaluate pancreatic segmentation performance. Dice per case score (DC) is the score obtained by averaging the scores of each slice, and dice global score (DG) is to calculate dice score after combining all predictions from a patient into a 3D volume. The calculation method is shown in Equation 11. Jaccard similarity coefficient (Jaccard) is similar to DSC to evaluate accuracy of the segmentation, whose expression is $J(X, Y) = (X \cap Y) / (|X| + |Y| - (X \cap Y))$.

We will also use four metrics to measure the accuracy of the segmentation results, including Root Mean Square Error (RMSE), which is the square root of the ratio of the sum of the observed and true deviations to the number n of observations. The deviation between the value and the true value, the expression is shown in Equation 12; the volume overlap error $VOE = 1 - vol(X \cap Y) / vol(X \cup Y)$; the relative volume difference $RVD = vol(Y \setminus X) / vol(X)$; False negative, $FN = vol(Y \setminus X) / vol(X \cup Y)$; False positive, $FP = vol(X \setminus Y) / vol(X \cup Y)$. The higher the number of Dice and Jaccard, the better the accuracy, and the smaller the remaining evaluation indicators, the better the segmentation result.

$$RMSE(x, y; \Omega) = \sqrt{\frac{1}{m} \sum_{i=1}^m (\Omega(x^i) - y^i)^2} \quad (12)$$

C. Implementation details

In this section, we will further describe the hardware conditions, experimental environment and model details. Our network is based on the Keras framework [36]. In order to prevent the model from entering the local minimum in training which makes model difficult to converge, we pay attention to the loss change in training process. If the loss does not decrease after two epochs, the learning rate lr will change according to the Equation 13-15 and Algorithm 2. If the value of loss on two consecutive epochs is less than the threshold δ (in this case, δ is 0.0001), the learning rate lr will be reduced to the $(1 - \beta)$ times of the original (in this case, β takes 0.9).

$$\mathcal{L} = [(|\mathcal{L}_i - \mathcal{L}_{i-1}| < \delta) \& (|\mathcal{L}_{i+1} - \mathcal{L}_i| < \delta)] \quad (13)$$

$$\xi(\lambda) = \begin{cases} 0, & \lambda \neq 1 \\ 1, & \lambda = 1 \end{cases} \quad (14)$$

$$lr = lr - lr \times (\beta \times \xi(\mathcal{L})) \quad (15)$$

Algorithm 2: The Function for Adjusting Loss

Input: loss value: $\ell \in R^{epoch}$, epsilon value: ε , patience value: p , adjustment factor: β ;

Output: adjusted lr : \tilde{lr} ;

1: $\varepsilon \leftarrow 0.0001, p \leftarrow 2, \beta \leftarrow 0.7, sign \leftarrow 1$;

2: **Repeat:**

3: $i \leftarrow 1$;

4: **For** j in range of $(i, p + i)$:

5: **If** $|\ell_{j-1} - \ell_j| > \varepsilon$:

6: $sign \leftarrow 0$;

7: **if** $sign$ is 1 after for loop, means all loss in

8: $(i, p + i)$ have no any drop more than ε ,

9: lr need to be adjusted.

10: **If** $sign == 1$:

11: $\bar{lr} = lr - lr \times \beta$;

12: $sign \leftarrow 1$;

13: $i \leftarrow i + p$;

14: **Until** $i == epoch$

Return: $\tilde{lr} \leftarrow \bar{lr}$

We train the probabilistic map extraction module on a NVIDIA GeForce GTX 1080Ti GPU with 11GB memory. The initial learning rate is e^{-5} , the batch_size is 10, the training epoch is 300. In each epoch, 1% of the samples are selected as the validation data to observe if over-fitting occurs. As for the bi-directional recurrent segmentation network, we use the same equipment to train. Because the label marked by the clinician is accurate enough, we used $(label_{i-1}, data_i, label_{i+1})$ as training data (the specific approach is consistent with that described in section B). The batch_size changed to 1, the number of training changed to 240. Other parameters, such as learning rates and optimization methods, are consistent with the previous.

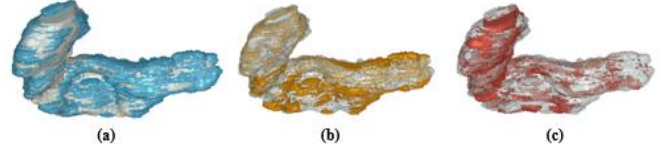


Fig. 6. The illustration of segmentation result, the gray part represents the ground truth. (a) The blue part represents the area of the error segmentation part; (b) The blue part represents the less segmentation part; (c) The yellow part represents the over segmentation part.

D. Quantitative and Qualitative Analysis

1) **Segmentation Result:** Experiments are carried out 10 times and 4-fold cross-validation method is employed. Figure 6 shows segmentation result, and Table I lists the DSC value. From Figure 6, we can see the result of our segmentation was excellent, with only some error segmentation in the edge of the pancreas. It can be seen that the mean DSC value of the proposed approach is 83.35%. With the bi-directional recurrent

segmentation, the result is increased by 2.03% and help the worst case get better (DSC value increases from 0% to 90% in some cases). Because of the guidance of context information from adjacent slices, the poor segmentation results of the middle layer can be easily optimized.

TABLE I: Evaluation results of segmentation on NIH dataset. Our model shows the competition performance compared to recent state-of-the-art pancreas segmentation methods.

Models	Year	Min DSC	Max DSC	Mean DSC
Roth et al., MICCAI'2015 [6]	2015	23.99	86.29	71.42 \pm 10.11
Roth et al., MICCAI'2016 [28]	2016	34.11	88.65	78.01 \pm 8.20
Dou et al., MIC'2017 [15]	2017	62.53	90.32	82.25 \pm 5.91
Zhou et al., MICCAI'2017 [5]	2017	62.43	90.85	82.37 \pm 5.68
Zhu et al., Arxiv'2017 [18]	2017	69.62	91.45	84.59 \pm 4.86
Ours		61.13	90.50	83.35 \pm 5.02

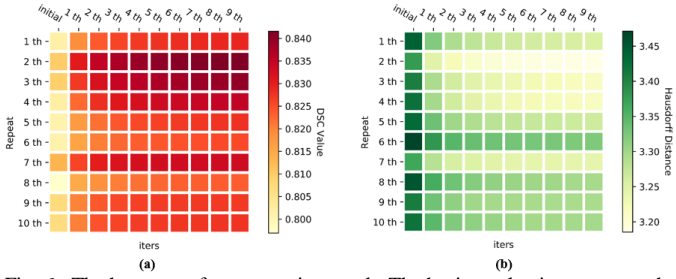


Fig. 6. The heatmap of segmentation result. The horizontal axis represents the number of iterations and the longitudinal axis represents the number of repeated experiments. A show that the increase of DSC by our proposed PBR-UNet; B show that the reduction of Hausdorff distance.

2) **The effectiveness of probabilistic map guidance:** In this section, we conduct comprehensive experiments to analyze the effectiveness of our proposed PBR-UNet. As can be seen from the iterative optimization process in Figure 7, the traditional UNet segmentation fails to segment these cases(the DSC value of initial segmentation result is 0, 0.67, 0.16), but with probabilistic map guidance, the result can reach a very competitive score (the DSC value of recurrent segmentation result is 0.90, 0.90, 0.88). Through the first iteration, the results of A, B and C in Figure 7 are increased by 0.86, 0.18 and 0.67 respectively, which shows important contribution to the final result. In addition, in order to verify the necessity of probabilistic map guidance, we use the binary image to carry on the comparison experiment. All parameters are consistent with the previous experiments to avoid introducing interference. We prove the necessity of using probabilistic map guidance by comparing the results of two models with different guidance. The results show that the DSC value of the segmentation guided by the probabilistic map are 1% higher than that guided by the binary image. It proves that the segmentation guided by probabilistic map can improve the segmentation results.

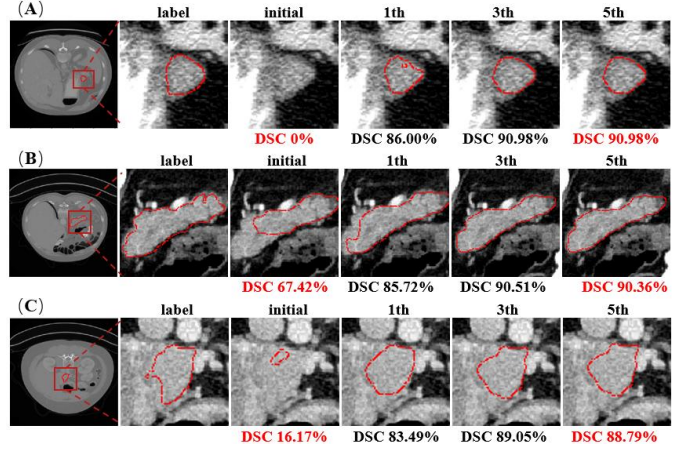


Fig. 7. The illustration of iterative optimization process. A, B and C in the figure denote the recurrent segmentation of 107th slice of patient 63, 115th slice of patient 15 and 160th slice of patient 40, respectively.

3) **The effectiveness of recurrent segmentation:** As we can see from the iteration process in Figure 7, although the results have been greatly improved after the first guided segmentation, there are some gaps compared to the standards. After the first guided segmentation, all the probabilistic maps were updated, the updated probability map still has the potential to improve the results. Therefore, we want to re-use the updated probabilistic maps for guiding. Inspired by the above ideas, we added a bi-directional recurrent segmentation process to take full advantage of the three-dimensional information generated by constantly updated probabilistic map. To demonstrate the effectiveness of our bidirectional iterations, we display the recurrent segmentation results for each iteration in the Figure 7. After a certain number of iterations, the pancreatic tissue boundary is getting closer to the standard, meaning that the iterative process is effective. We can get stable results after 5 iterations. Figure 8 shows the relationship between the number of iterations and accuracy, and we can see that after 10 iterations, the results have been very stable, which indicates that three-dimensional information has been fully propagated in the recurrent process.

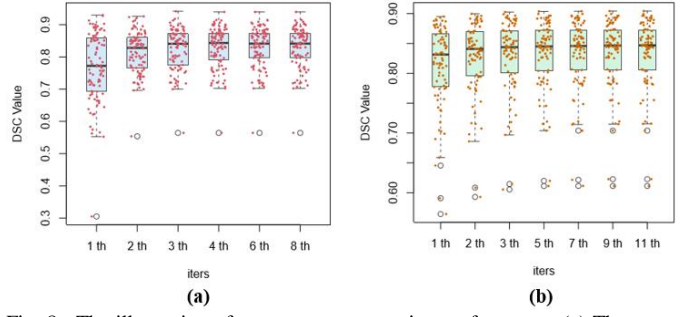


Fig. 8. The illustration of recurrent segmentation performance. (a) The mean DSC value of No.8 patient. (b) The mean DSC value of all test patient.

4) **The effectiveness of using adjacent slice:** We chose to use the adjacent three slices as input in the recurrent segmentation module. All slices of the entire pancreas are divided into a certain number of interrelated three-channel data. The interaction between these adjacent three-channel data forms an interlocking structure. From the Figure 9, we can see that under the guidance of 123th slice and 125th slice, the 124th

slice as the middle slice has been greatly improved. The 123th and 125th slice can also be guided by their adjacent slices, so there will be some increase in the final segmentation results. The adjacent three slices shown in Figure 9 end up with more than 86% of the final segmentation results. What's more, we also conducted comparative experiments to explore the impact of the depth of guidance on the results. In previous experiments, the guidance depth in the three-channel data was only 1, and now we increase the depth to 2 to turn three-channel data into five-channel data. Both two experiments were conducted under the same experimental settings. As can be seen from the Table II, increasing the guidance depth to 2 results in a worse result because the increase in depth introduces more interference information, and we infer that the deeper the depth, the worse the effect. As we can see from Figure 1, the pancreas is highly shape-specific, and an increase in guidance depth will allow this specificity to move more into the segmentation model, leading to worse results.

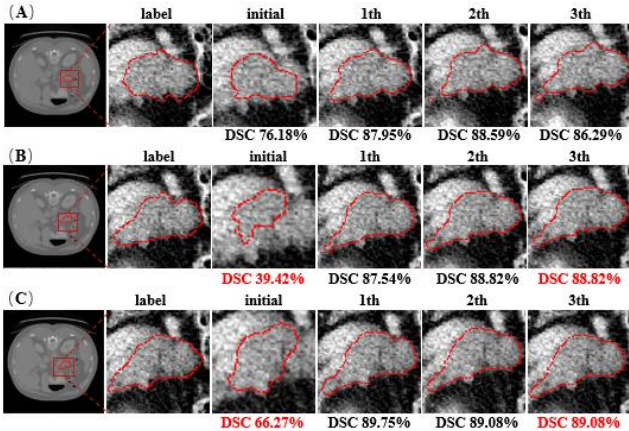


Fig. 9. The illustration of an iterative optimization process for adjacent three slices. A, B and C in the figure denote the recurrent segmentation of 123th slice, 124th slice and 125th slice of patient 63, respectively.

5) **The reliability of PBR-UNet:** Because the size of the pancreas is small in CT scans, there are even some examples where the pancreatic region accounts for only 1% of the entire slice, the segmentation results for partial sections are less than 40%. As shown in Figure 5, our model can assist the segmentation of middle slice through the upper and lower slice, so that the slice with a better segmentation result can be used to improve the output of those poor slices of results. Thus, we counted the number of slices in the experiment with less than 40% segmentation accuracy to verify the ability of our model to improve the poor situation. As shown in Figure 10, in the segmentation result using standard UNet, the number of slices with a DSC value of less than 40% reached 368. The number of slices less than 40% in our proposed PBR-UNet segmentation results is reduced to only 230. And most of these slices are distributed at the edge of the pancreas, making it difficult to use the upper and lower levels of information for guided segmentation. As can be seen from the linear regression graph (c, d) in Figure 10, compared with the standard UNet, there is a stronger correlation between the segmentation results of our proposed PBR-UNet and the reference standards.

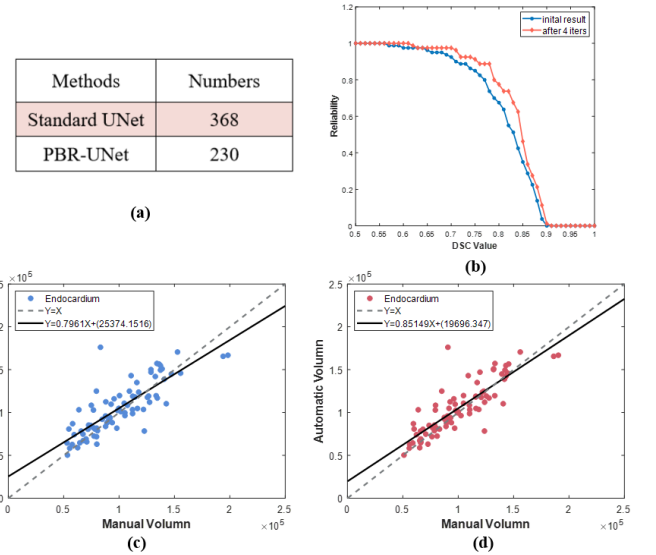


Fig. 10. The illustration of reliability performance. (a) Number of segmentation results DSC value less than 10%. (b) The display of model reliability, horizontal coordinates represent DSC value, and longitudinal coordinates represent a percentage greater than the corresponding DSC value in the result. (c) Segmentation volumes of standard UNet versus manual volumes. (d) Segmentation volumes of our proposed PBR-UNet versus manual volumes.

E. Time consumption

Our proposed bi-directional recurrent network based on probabilistic map guidance is a lightweight solution with low computational resource occupation and low time resource overhead. We conducted a comparison of experimental time with other models. We can see that we only need 15 s to test a patient's result, which is much shorter than the models using the refine methods such as CRF and BiLSTM.

IV. DISCUSSION

Pancreas segmentation is of great significance for clinical computer-aided diagnosis. The segmentation results can provide accurate location and contour of the pancreas, which is helpful to the clinical diagnosis process. In this paper, we present a probabilistic map guided segmentation network, which aims to explore contextual information without too much computational resource. Our proposed PBR-UNet has achieved a competitive result. The overhead of our network's time resources is very low, which is important in clinical practice, especially when 3D images in large size or multiple slices are increasingly used in clinical applications [14]. We adopted a basic 3D UNet network [19] to verify whether our computing resources can meet all requirements. We experimented on two NVIDIA GeForce GTX 1080Ti GPU with 11GB memory. The network is a four-layer network with symmetrical structure. The size of the input data is $120 \times 120 \times 120$, but we still encountered the error of insufficient memory. By contrast, our network can work well with only one such device under the same parameters. In terms of resource consumption, the use of 3D UNet will make it higher, so our approach is more clinically practical.

To better understand the validity of the model, we also compared individual patients, in which the highest accuracy can be improved 7% for patients. To verify the rigor of this

method, we carried out an experiment with two adjacent layers of the pancreas as guidance. We can see that the introduction of the adjacent two layers can increase the intensity of guidance compared with adjacent layer. However, it will also introduce irrelevant interference. It is noteworthy that in some cases the accuracy of certain layers of the pancreas is very low, especially in the head and tail of the pancreas. This is one of the directions we will strive for and we hope to solve the edge effect in segmentation. Due to lack part of the context information on the edge, unsatisfactory segmentation results in several layers are often caused.

V. CONCLUSION

We propose a probabilistic map guided bi-directional recurrent network PBR-UNet for pancreas segmentation, which is a new way to get context information and propagate context information to the entire network. It is a lightweight approach to overcome the drawbacks of consuming excessive resources in 3D networks and ignoring Z-axis contextual information in 2D networks. Extensive experiments on the dataset of NIH Pancreas dataset demonstrated the superiority of our proposed PBR-UNet, and finally achieve a competitive result of 83.35%.

REFERENCES

- [1] C. Chu *et al.*, “Multi-organ segmentation based on spatially-divided probabilistic atlas from 3D abdominal CT images,” *Lect. Notes Comput. Sci. (including Subser. Lect. Notes Artif. Intell. Lect. Notes Bioinformatics)*, vol. 8150 LNCS, no. PART 2, pp. 165–172, 2013.
- [2] R. Wolz, C. Chu, K. Misawa, M. Fujiwara, K. Mori, and D. Rueckert, “Automated abdominal multi-organ segmentation with subject-specific atlas generation,” *IEEE Trans. Med. Imaging*, vol. 32, no. 9, pp. 1723–1730, 2013.
- [3] Y. Man, Y. Huang, J. Feng, X. Li, and F. Wu, “Deep Q Learning Driven CT Pancreas Segmentation with Geometry-Aware U-Net,” no. December, pp. 0–10, 2018.
- [4] H. R. Roth, A. Farag, L. Lu, E. B. Turkbey, and R. M. Summers, “Deep convolutional networks for pancreas segmentation in CT imaging,” no. March 2015, 2015.
- [5] Y. Zhou, L. Xie, W. Shen, Y. Wang, E. K. Fishman, and A. L. Yuille, “A fixed-point model for pancreas segmentation in abdominal CT scans,” *Lect. Notes Comput. Sci. (including Subser. Lect. Notes Artif. Intell. Lect. Notes Bioinformatics)*, vol. 10433 LNCS, pp. 693–701, 2017.
- [6] H. R. Roth *et al.*, “Deeporgan: Multi-level deep convolutional networks for automated pancreas segmentation,” *Lect. Notes Comput. Sci. (including Subser. Lect. Notes Artif. Intell. Lect. Notes Bioinformatics)*, vol. 9349, pp. 556–564, 2015.
- [7] E. Shelhamer, J. Long, and T. Darrell, “Fully Convolutional Networks for Semantic Segmentation,” pp. 1–12, 2016.
- [8] O. Ronneberger, P. Fischer, and T. Brox, “U-Net: Convolutional Networks for Biomedical Image Segmentation,” pp. 1–8, 2015.
- [9] L. C. Chen, G. Papandreou, I. Kokkinos, K. Murphy, and A. L. Yuille, “DeepLab: Semantic Image Segmentation with Deep Convolutional Nets, Atrous Convolution, and Fully Connected CRFs,” *IEEE Trans. Pattern Anal. Mach. Intell.*, vol. 40, no. 4, pp. 834–848, 2018.
- [10] M. Drozdzal, E. Vorontsov, G. Chartrand, S. Kadoury, and C. Pal, “The Importance of Skip Connections in Biomedical Image Segmentation,” 2016.
- [11] G. González, G. R. Washko, and R. San José Estépar, “Multi-structure Segmentation from Partially Labeled Datasets. Application to Body Composition Measurements on CT Scans,” in *Image Analysis for Moving Organ, Breast, and Thoracic Images*, 2018, pp. 215–224.
- [12] J. Cai, L. Lu, F. Xing, and L. Yang, “Pancreas Segmentation in CT and MRI Images via Domain Specific Network Designing and Recurrent Neural Contextual Learning,” no. Cv, pp. 1–11, 2018.
- [13] J. Cai, L. Lu, Y. Xie, F. Xing, and L. Yang, “Improving Deep Pancreas Segmentation in CT and MRI Images via Recurrent Neural Contextual Learning and Direct Loss Function,” pp. 1–8, 2017.
- [14] X. Li, H. Chen, X. Qi, Q. Dou, C. W. Fu, and P. A. Heng, “H-DenseUNet: Hybrid Densely Connected UNet for Liver and Tumor Segmentation from CT Volumes,” *IEEE Trans. Med. Imaging*, no. 1, pp. 1–13, 2018.
- [15] Q. Dou, H. Chen, Y. Jin, L. Yu, J. Qin, and P.-A. Heng, “3D Deeply Supervised Network for Automatic Liver Segmentation from CT Volumes,” in *Medical Image Computing and Computer-Assisted Intervention -- MICCAI 2016*, 2016, pp. 149–157.
- [16] O. Oktay *et al.*, “Attention U-Net: Learning Where to Look for the Pancreas,” no. Midl, 2018.
- [17] S. Liu *et al.*, “3D anisotropic hybrid network: Transferring convolutional features from 2D images to 3D anisotropic volumes,” *Lect. Notes Comput. Sci. (including Subser. Lect. Notes Artif. Intell. Lect. Notes Bioinformatics)*, vol. 11071 LNCS, pp. 851–858, 2018.
- [18] Z. Zhu, Y. Xia, W. Shen, E. Fishman, and A. Yuille, “A 3D coarse-to-fine framework for volumetric medical image segmentation,” *Proc. - 2018 Int. Conf. 3D Vision, 3DV 2018*, pp. 682–690, 2018.
- [19] Ö. Çiçek, A. Abdulkadir, S. S. Lienkamp, T. Brox, and O. Ronneberger, “3D U-net: Learning dense volumetric segmentation from sparse annotation,” *Lect. Notes Comput. Sci. (including Subser. Lect. Notes Artif. Intell. Lect. Notes Bioinformatics)*, vol. 9901 LNCS, pp. 424–432, 2016.
- [20] F. Milletari, N. Navab, and S. A. Ahmadi, “V-Net: Fully convolutional neural networks for volumetric medical image segmentation,” *Proc. - 2016 4th Int. Conf. 3D Vision, 3DV 2016*, pp. 565–571, 2016.
- [21] Z. Quo *et al.*, “Deep LOGISMOS: Deep learning graph-based 3D segmentation of pancreatic tumors on

CT scans,” *Proc. - Int. Symp. Biomed. Imaging*, vol. 2018–April, no. Isbi, pp. 1230–1233, 2018.

[22] Q. Jin, Z. Meng, C. Sun, L. Wei, and R. Su, “RA-UNet: A hybrid deep attention-aware network to extract liver and tumor in CT scans,” no. October, pp. 1–13, 2018.

[23] C. Chung *et al.*, “Very deep convolutional networks for large-scale image recognition,” *Comput. Sci.*, 2014.

[24] M. Lai, “Deep Learning for Medical Image Segmentation,” 2017. [Online]. Available: <https://arxiv.org/abs/1505.02000>.

[25] P. F. Christ *et al.*, “Automatic Liver and Lesion Segmentation in CT Using Cascaded Fully Convolutional Neural Networks and 3D Conditional Random Fields,” in *Medical Image Computing and Computer-Assisted Intervention -- MICCAI 2016*, 2016, pp. 415–423.

[26] H. R. Roth *et al.*, “An application of cascaded 3D fully convolutional networks for medical image segmentation,” *Comput. Med. Imaging Graph.*, vol. 66, no. March, pp. 90–99, 2018.

[27] M. Tang, Z. Zhang, D. Cobzas, M. Jagersand, and J. L. Jaremko, “Segmentation-by-detection: A cascade network for volumetric medical image segmentation,” *Proc. - Int. Symp. Biomed. Imaging*, vol. 2018–April, no. Isbi, pp. 1356–1359, 2018.

[28] H. R. Roth *et al.*, “Spatial aggregation of holistically-nested convolutional neural networks for automated pancreas localization and segmentation,” *Med. Image Anal.*, vol. 45, pp. 94–107, 2018.

[29] Q. Yu, L. Xie, Y. Wang, Y. Zhou, E. K. Fishman, and A. L. Yuille, “Recurrent Saliency Transformation Network: Incorporating Multi-Stage Visual Cues for Small Organ Segmentation,” vol. 2, 2017.

[30] X. Yang *et al.*, “Towards Automated Semantic Segmentation in Prenatal Volumetric Ultrasound,” *IEEE Trans. Med. Imaging*, vol. PP, no. c, pp. 1–1, 2018.

[31] Y. Hua, L. Mou, and X. X. Zhu, “Recurrently Exploring Class-wise Attention in A Hybrid Convolutional and Bidirectional LSTM Network for Multi-label Aerial Image Classification,” 2018.

[32] A. Krizhevsky, I. Sutskever, and G. E. Hinton, “ImageNet Classification with Deep Convolutional Neural Networks,” *Adv. Neural Inf. Process. Syst.*, pp. 1–9, 2012.

[33] M. D. Zeiler and R. Fergus, “Visualizing and Understanding Convolutional Networks,” in *Computer Vision -- ECCV 2014*, 2014, pp. 818–833.

[34] Y. Xia *et al.*, “3D Semi-Supervised Learning with Uncertainty-Aware Multi-View Co-Training,” 2018.

[35] I. Goodfellow, Y. Bengio, and A. Courville, *Deep Learning*. The MIT Press, 2016.

[36] F. Chollet *et al.*, “Keras,” <https://github.com/keras-team/keras>, 2015.